Journal of Materials Chemistry C

ROYAL SOCIETY OF CHEMISTRY

PAPER

View Article Online
View Journal | View Issue

Cite this: J. Mater. Chem. C, 2025, 13, 12812

Exploring the balance between spin frustration and single-ion effects in triangular Dy_3 complexes†

Chieh-Wei Chang,[a] Jérôme Rouquette,[b] Po-Heng Lin *[a] and Jérôme Long *[bc]

Received 23rd January 2025,
Accepted 15th May 2025

DOI: 10.1039/d5tc00334b

rsc.li/materials-c

We report the synthesis, structures, and magnetic properties of a series of triangular Dy_3 complexes with $[Dy_3(hmci)_3(MeOH)_6]\cdot 3MeOH\cdot 2MeCN\cdot 2H_2O$ (**1**) and $[Dy_3(hmcb)_3(MeOH)_6]\cdot 3MeOH\cdot 1H_2O$ (**2**) (H_3hmci = 2-hydroxy-3-methoxy-5-iodobenzaldehyde hydrazone, H_3hmcb = 2-hydroxy-3-methoxy-5-bromobenzaldehyde hydrazone). These complexes adopt a calixarene-like triangular topology with phenoxide-bridged Dy^{3+} ions, leading to near-perpendicular orientation of anisotropic axes relative to the Dy_3 plane. Magnetic studies and theoretical calculations reveal rare examples of Ising spin frustration driven by dipolar interactions, while retaining a zero-field single-molecule-magnet (SMM) behavior. Furthermore, halogen substitutions at the *para* position of the ligands fine-tune the local crystal field environment, enabling modulation of the relaxation dynamics and slow magnetic relaxation profiles. These findings underscore the critical role of ligand design in tailoring spin frustration and optimizing the zero-field SMM performance of triangular Dy_3 complexes.

1. Introduction

Single-molecule magnets (SMMs) are a remarkable class of molecular materials celebrated for their ability to exhibit slow relaxation of magnetization and magnetic hysteresis at the molecular level, driven by strong magnetic anisotropy. Over the years, SMMs have shown tremendous potential for applications in quantum computing, high-density data storage, and spintronic devices.[1–6] While lanthanide-based mononuclear systems have provided fundamental insights into SMM behavior, particularly through precise control of magnetic anisotropy *via* chemical manipulation of crystal-field (CF) splitting, especially for Dy^{3+} ions,[7–19] further progress depends on addressing limitations imposed by spin–phonon interactions. In particular, Raman relaxation, which can hinder performance by reducing the blocking temperature, has emerged as a critical bottleneck.[20–23]

In parallel, magnetic interactions between lanthanide ions in polynuclear complexes introduce additional layers of complexity and opportunities for tuning their magnetic properties.[23] These interactions influence key parameters such as blocking temperature and magnetic coercivity, often balancing the subtle dipolar and exchange contributions.[24–30]

Among polynuclear complexes, triangular Dy_3 complexes have emerged as ideal models for exploring the interplay between magnetic anisotropy and intramolecular magnetic interactions.[31] This topology offers an intriguing platform where the spatial arrangement of Dy^{3+} ions and their anisotropic axes can create unique magnetic behaviors such as vortex-like arrangements of magnetic moments, resulting in toroidal moments with nonmagnetic ground states but retaining fascinating dynamic properties like slow relaxation and quantum tunnelling.[32–36] Thus, the magnetic interactions between Dy^{3+} ions, mediated by the surrounding ligands in combination with the relative orientation of the local anisotropic axis play a critical role in determining the overall magnetic behavior and relaxation dynamics. Beyond their magnetic properties, Dy_3 triangles have also drawn attention for their potential to exhibit magnetoelectric coupling, expanding the scope of molecular materials with coupled ferroic properties.[37]

Spin frustration in an Ising triangle, on the other hand, arises from competing antiferromagnetic interactions, which in molecular systems such as triangular trinuclear complexes, lead to nearly degenerate spin ground states.[38–40] The ideal

[a] Department of Chemistry, National Chung Hsing University, Taichung 402, Taiwan. E-mail: poheng@dragon.nchu.edu.tw
[b] ICGM, Univ. Montpellier, CNRS, ENSCM, Montpellier, France. E-mail: jerome.long@umontpellier.fr
[c] Institut Universitaire de France (IUF), 1 rue Descartes, 75231 Paris Cedex 05, France

† Electronic supplementary information (ESI) available: Additional structural and magnetic and *ab initio* calculations data. CCDC 2412858 and 2412859. For ESI and crystallographic data in CIF or other electronic format see DOI: https://doi.org/10.1039/d5tc00334b

frustrated Ising triangle requires a perfectly equilateral geometry, with principal magnetic axes perpendicular to the triangle's plane and sufficiently large Dy^{3+}–Dy^{3+} distances to suppress exchange interactions. In such a configuration, dipolar interactions dominate and induce a frustrated ground state. Yet achieving this necessitates precise control over the orientation of the anisotropic axes as dipolar interactions among highly anisotropic magnetic centers play a critical role in the relaxation dynamics in polynuclear SMMs. Traditionally viewed as either negligible or detrimental, these interactions, when carefully tuned, can effectively govern transition probabilities between low-energy states.[41,42] This highlights their potential as a strategic mechanism for refining relaxation processes and tailoring magnetic properties in complex systems.

In this context, phenoxide-based ligands have been widely utilized for assembling polynuclear SMMs with high energy barriers, offering a robust framework for constructing diverse core topologies.[2,5,16,43–50] Previously, we reported a triangular Dy_3 complex based on the H_3hnc (1,5-bis(2-hydroxy-3-methoxy-5-nitrobenzylidene)carbonohydrazide) featuring an electron-withdrawing NO_2 group in the *para* position.[31] This topology features a central Dy_3 triangle with *para*-substituents projecting outward in a tripod-like configuration below the Dy_3 plane.

Building on this foundation, the present study extends this design by incorporating halogen substituents. In contrast to our previous work with a NO_2 π-withdrawing group, we utilize halogen substituents, known for their π-donating ability, with the aim to increase the electron density at the phenoxide oxygen and in turn modulate the magnetic anisotropy and relaxation dynamics. By examining the steric and electronic effects introduced by halogen variations, we aim to uncover how these subtle modifications govern the magnetic behavior in two novel triangular Dy_3 SMMs and in particular their spin frustration. Interestingly, despite differences in ligand substitution and the number of crystallographically distinct Dy^{3+} centers, a similar low-temperature regime observed in our earlier study is evident. This finding suggests a consistent underlying behavior in these systems. This work underscores the adaptability of the tripod-like arrangement while offering a strategic framework for optimizing SMM performance through tailored ligand design.

2. Experimental

2.1. General conditions

All chemicals and solvents were purchased from Alfa Aesar, and used as received without further purification. The 2-hydroxy-5-iodo-3-methoxybenzaldehyde was prepared according to literature procedures by *o*-vanillin reacting with iodine monochloride.[51] The 5-bromo-2-hydroxy-3-methoxy-benzaldehyde was prepared according to literature procedures by reacting with *o*-vanillin, sodium acetate and bromine in glacial acetic acid.[52] 1 H spectra were recorded on a Varian Mercury-400 (400 MHz for 1 H) spectrometer. Infrared spectra were recorded on all samples in the solid-state under ambient conditions on a Nicolet iS5 FT-IR spectrometer with iD5-ATR accessory in the 4000–400 cm^{-1} region.

2.2. Synthesis of the ligands (H_3hmci and H_3hmcb)

2-Hydroxy-5-iodo-3-methoxybenzaldehyde/5-bromo-2 hydroxy-3-methoxy-benzaldehyde (20 mmol) was added to EtOH (100 mL), followed by the addition of carbohydrazide (10 mmol). The solution was refluxed at 70 °C for 3 hours. A white precipitate formed as the product, which was collected by filtration after removing the remaining ethanol. The precipitate was washed with water and dried under vacuum.

H_3hmci: yield = 80.4%. NMR (DMSO-d_6, 400 MHz): 10.95 (s, 2H), 8.37 (s, 2H), 7.70 (s, 2H), 7.2 (dd, 2H), 3.81 (s, 6H). IR (ATR cm^{-1}): 1699 (s), 1612 (w), 1592 (w), 1563 (m), 1530 (s), 1485 (s), 1439 (m), 1413 (m), 1350 (m), 1265 (s), 1245 (s), 1213 (s), 1143 (m), 1078 (m), 1017 (w), 943 (w), 842 (w), 832 (w).

H_3hmcb: yield: 79.2%. NMR (DMSO-d_6, 400 MHz): 10.98 (s, 2H), 8.40 (s, 2H), 7.56 (s, 2H), 7.11 (dd, 2H), 3.83 (s, 6H). IR (ATR cm^{-1}): 1605 (w), 1573 (w), 1473 (s), 1449 (m), 1439 (m), 1422 (s), 1402 (w), 1352 (m), 1318 (w), 1214 (s), 1139 (w), 1101 (w), 1074 (s), 1005 (w), 927 (m), 847 (m), 824 (s), 784 (m), 761 (s), 700 (m).

2.3. Synthesis of $[Dy_3(hmci)_3(MeOH)_6]\cdot 3MeOH\cdot 2MeCN\cdot 2H_2O$ ($1\cdot 3MeOH\cdot 2ACN\cdot 2H_2O$)

To a solution of $DyCl_3\cdot 6H_2O$ (0.125 mmol) in MeOH/MeCN (11.5 mL/3.5 mL) was added a solution of H_3hmci (0.125 mmol, 0.0762 g), and tetraethylammonium hydroxide (0.5 mmol, 0.205 mL) in MeOH/MeCN (11.5 mL/3.5 mL). The solution was stirred for 1 min and then filtered. The yellow solution was left to settle for one week, after which transparent yellow crystals of **1** were obtained by filtration, washed with ether, and dried *in vacuo*. Complex **1**: yield = 9.31%. IR (ATR cm^{-1}): 1594 (w), 1560 (m), 1488 (s), 1456 (s), 1439 (s), 1379 (s), 1306 (m), 1231 (s), 1212 (s), 1148 (w). 1113 (m), 1078 (m), 1020 (w), 956 (w), 863 (w), 837 (w), 779 (m), 760 (s), 713 (m), 663 (m). Anal. (%) calcd for $C_{57}H_{75}N_{12}Dy_3O_{27}I_6$(**1**·$6H_2O$): C, 26.24; H, 2.90; N, 6.44. Found: C, 25.99; H, 2.62; N, 6.69. CCDC number: 2412859.†

2.4. Synthesis of $[Dy_3(hmcb)_3(MeOH)_6]\cdot 3MeOH\cdot 1H_2O$ ($2\cdot 3MeOH\cdot 1H_2O$)

To a solution of $Dy(OAc)_3\cdot 4H_2O$ (0.125 mmol) in MeOH (15 mL) was added a solution of H_3hmcb (0.125 mmol, 0.0645 g), and triethylamine (1 mmol, 0.139 mL) in MeOH (15 mL). The solution was stirred for 1 min and then filtered. The yellow solution was left to settle for one week, after which transparent yellow crystals of **2** were obtained by filtration, washed with ether, and dried *in vacuo*. Complex **2**: Yield = 16.56%. IR (ATR cm^{-1}): 1596 (w), 1561 (m), 1541 (w), 1488 (s), 1456 (s), 1440 (s), 1408 (w), 1377 (s), 1304 (m), 1229 (s), 1209 (s), 1147 (w), 1079 (m), 955 (w), 839 (w), 805 (w), 786 (m), 760 (s), 721 (m), 669 (m). Anal. (%) calcd for $C_{57}H_{79}N_{12}Dy_3O_{29}Br_6$(**2**·$8H_2O$): C, 28.97; H, 3.37; N, 7.11. Found: C, 28.63; H, 3.03; N, 7.22. CCDC number: 2412858.†

2.5. X-ray crystallography

Single crystals of complexes **1–2** suitable for X-ray diffraction measurements were mounted on an Oxford Xcalibur Sapphire-3 CCD Gemini diffractometer employing graphite-monochromated Mo-Kα radiation (λ = 0.71073 Å), and intensity data were collected with ω scans. The data collection and reduction were performed with the CrysAlisPro software, and the absorptions were corrected by the SCALE3 ABSPACK multiscan method. The space-group determination was based on a check of the Laue symmetry and systematic absences, and it was confirmed using the structure solution. The structure was solved and refined with the *Olex2 1.2-ac21* package. Anisotropic thermal parameters were used for all non-H atoms, and fixed isotropic parameters were used for H atoms.

Powder diffraction patterns were collected on a Bruker AXS D8 Advance X-ray diffractometer using Cu Kα radiation (λ = 1.5418 Å). XRD data were collected within a 2θ range of 5 to 40°.

2.6. Magnetic measurements

Magnetic susceptibility data were collected with a Quantum Design MPMS3 SQUID magnetometer working in the range 1.8–300 K with the magnetic field up to 7 Tesla. The samples were filtered and prepared immediately prior to the magnetic measurements in order to minimize any potential degradation. The data were corrected from the sample holder and the diamagnetic contributions calculated from the Pascal's constants. The AC magnetic susceptibility measurements were carried out in the presence of a 2.5 Oe oscillating field in zero or applied external DC field.

2.7. Theoretical calculations

CASSCF calculations were performed with ORCA 6.0[53,54] software using the crystallographic structures without any structural geometry optimization. For $[Dy_3(hnc)_3(DMF)_6]$,[31] the molecular orientation was redefined to properly account for the C_3 symmetry between the Dy^{3+} sites, ensuring that this axis was aligned along the *z*-direction and perpendicular to the Dy_3 plane. This redefinition was achieved by transforming the $Pa\bar{3}$ (205) space group into the $R\bar{3}$ (148) space group using the transformation matrix $a - b$, $b - c$, $a + b + ca - b$, $b - c$, $a + b + ca - b$, $b - c$, $a + b + c$ as provided by the Bilbao Crystallographic Serveer.[55,56] Tolerance for energy convergence is fixed at 10^{-7} E_h. An active space considering the seven 4f orbitals with 9 electrons CAS (9, 7) for all the sextets (21 roots) for spin–orbit coupling using QDPT was considered. The calculations employed the def2 Ahlrichs basis sets: DKH-DEF2-TZVP for all atoms except Dy, for which the SARC2-DKH-QZVP basis set was used, and Y, for which the SARC-DKH-TZVP basis set was applied. The AUTOAUX feature was used to automatically generate auxiliary basis sets within the RIJCOSX approximation to speed up the calculations. Then, the SINGLE_ANISO and POLY_ANISO[57] program implemented in ORCA was used to obtain details about the magnetic relaxation.

3. Results and discussions

3.1. Synthesis and crystal structures

To achieve the goal of synthesizing polynuclear complexes with unique topologies, we use the *o*-vanillin building-block to design ligands with multiple coordination sites (Scheme 1). In our previous study, Dy-based trinuclear SMMs were successfully synthesized using Schiff base ligands incorporating several coordination pockets.[31] Building on this foundation, the ligands in this study were strategically modified with -I and -Br substituents at the *para* position of *o*-vanillin to investigate how subtle changes in ligand chemistry influence magnetic properties while maintaining similar coordination environments.

The triangular Dy_3 complexes, $[Dy_3(hmci)_3(MeOH)_6]\cdot 3MeOH\cdot 2MeCN\cdot 2H_2O$ (**1**) and $[Dy_3(hmcb)_3(MeOH)_6]\cdot 3MeOH\cdot 1H_2O$ (**2**), were synthesized *via* straightforward one-pot reactions conditions.

Both reactions utilized a 1 : 1 molar ratio of the Dy^{3+} precursor and the corresponding Schiff-base ligand (H_3hmci or H_3hmcb) in methanolic solutions with an excess of base. Methanol served dual roles, acting as the solvent and a terminal ligand occupying coordination sites on the Dy_3 core.

For complex **1**, $DyCl_3\cdot 6H_2O$ was used as the metal precursor, and tetraethylammonium hydroxide (TEAOH, 3.8 equiv.) served as the base to facilitate the deprotonation of H_3hmci and promote the formation of the triangular assembly. While the reaction of H_3hmcb with $DyCl_3\cdot 6H_2O$ and TEAOH yielded microcrystalline powders, substituting $DyCl_3\cdot 6H_2O$ with $Dy(OAc)_3\cdot 4H_2O$ and TEAOH with triethylamine (NEt_3, 8 equiv.) afforded yellow crystals of **2**.

The choice of ligand substituents (–I in H_3hmci *vs.* –Br in H_3hcmb), the base, its quantity, and the Dy^{3+} precursor anions (although not incorporated into the structure) all influenced the crystallization behavior. Unfortunately, attempts to crystallize the system with the chlorine-ligand analogue were unsuccessful.

X-ray analysis reveals that complexes **1** and **2** crystallize in the triclinic $P\bar{1}$ space group with a trinuclear complex in the asymmetric unit (Table S1, ESI†). Both structures consist of triangular $[Dy_3(hmci/hmcb)_3(MeOH)_6]$ complexes, where three crystallographically independent Dy^{3+} ions, labelled Dy_1, Dy_2, and Dy_3, are interconnected by the central part of the ligand *via* three nitrogen atoms and one alkoxide moiety (Fig. 1 and Fig. S1, ESI†). The intramolecular Dy^{3+}–Dy^{3+} distances range from 5.772 to 5.873 Å in **1**, while slightly shorter ranges are

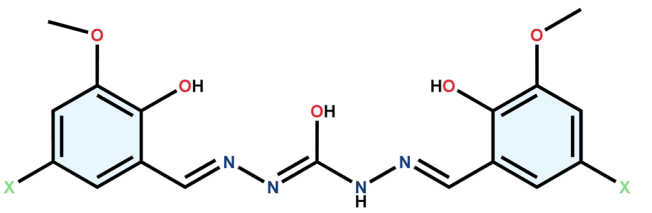

H_3hmci, X = I
H_3hmcb, X = Br

Scheme 1 Scheme of the H_3hmci and H_3hmcb ligands.

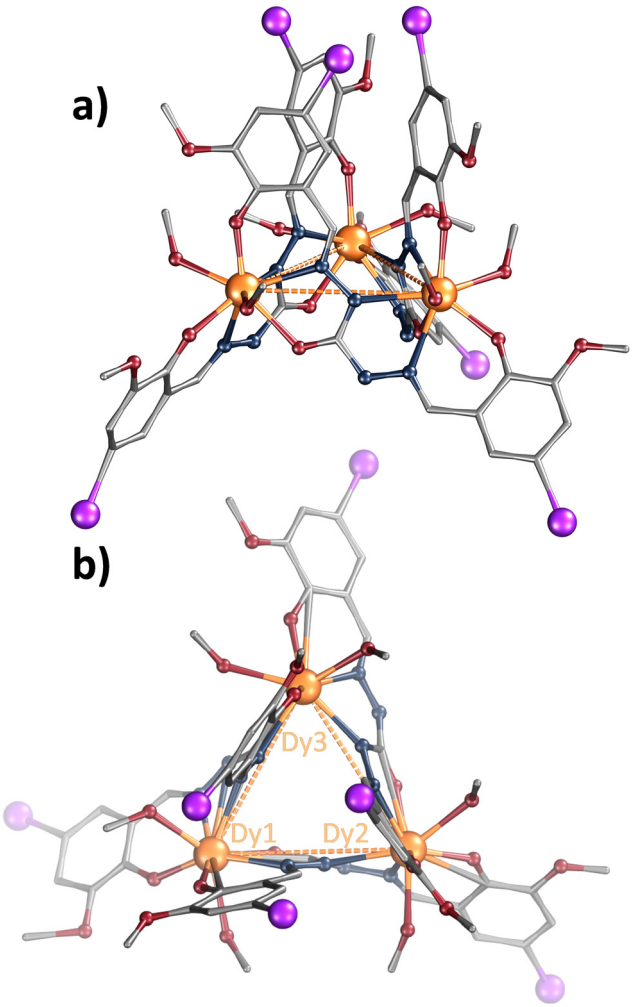

Fig. 1 (a) Molecular structures of **1**. Colour code: orange, Dy; red, O; blue, N; grey, C.; purple, I. Hydrogen atoms have been omitted for clarity. (b) View from the top of the Dy_3 triangle arrangement.

Table 1 Some relevant crystallographic parameters for **1–3**

Compound	Dy–O terminal (Å) out of plane	Dy–O terminal (Å) in-plane	O–Dy–O	Dy–Dy distances (Å)
1	2.184(12)	2.243(12)	116.0(5)	5.772
	2.218(12)	2.240(14)	110.6(5)	5.779
	2.166(12)	2.196(15)	110.8(5)	5.873
2	2.204(5)	2.271(5)	106.32(17)	5.758
	2.226(4)	2.255(5)	114.93(17)	5.798
	2.221(5)	2.213(4)	118.17(18)	5.896

observed in **2** (5.758 to 5.896 Å), indicating subtle structural variations (Table 1). Each Dy^{3+} ion exhibits eight-coordinate geometry, coordinated by three nitrogen and three oxygen atoms from the hmci/hmcb ligands, along with two methanol molecules. However, SHAPE analysis[58] highlights distinct differences in coordination geometries between complexes **1** and **2** (Table S2, ESI†). In **1**, all Dy^{3+} ions adopt a dodecahedral geometry with varying degrees of distortion, with Dy_2 exhibiting the lowest degree of distortion. In contrast, complex **2** shows Dy_1 and Dy_2 in a dodecahedral geometry, while Dy_3 adopts a distorted biaugmented trigonal prism.

Two short Dy–O(phenoxide) bonds from distinct ligands are notable in both complexes. The Dy–O bonds nearly perpendicular to the Dy_3 triangular plane measure 2.166–2.185 Å in **1** and 2.199–2.227 Å in **2**, while those within the plane are slightly longer, ranging from 2.196–2.243 Å in **1** and 2.209–2.275 Å in **2**. The angles between these bonds further emphasize the geometric differences, ranging from 105° to 116° in **1** and 106.25° to 118.31° in **2** (Table 1). Hydrogen bonding interactions are evident within the structures and are observed between the ligands and coordinated methanol molecules. The shortest intermolecular Dy^{3+}–Dy^{3+} distance in the crystal is 7.601 Å, indicating a relatively close packing (Fig. S2, ESI†).

PXRD measurements show that the compounds rapidly lose crystallinity upon exposure to air (Fig. S3, ESI†).

3.2. Magnetic properties

The magnetic properties of the triangular complexes were investigated using SQUID magnetometry under both static and dynamic conditions.

At room temperature, the χT (χ being the molar magnetic susceptibility and T the temperature) values for complexes **1** and **2**, were determined to be 42.08 cm^3 K mol^{-1} and 42.44 cm^3 K mol^{-1}, respectively. These values align well with the theoretical value of 42.51 cm^3 K mol^{-1} expected for three isolated Dy^{3+} ion ($^6H_{15/2}$) (Fig. 2).

Upon cooling, the thermal dependence of χT reveals a gradual decrease, reaching 27.04 cm^3 K mol^{-1} for **1** and 28.02 cm^3 K mol^{-1} for **2** at 1.8 K. This decrease is attributed to the thermal depopulation of the $\pm m_J$ levels, potentially combined with dominant antiferromagnetic interactions between the Dy^{3+} ions. The field-dependent magnetization curves, measured up to 70 kOe at 1.8 K, exhibit unsaturated behavior for both complexes, indicative of significant magnetic anisotropy (Fig. 2, inset). The magnetization (M) values at 70 kOe are 15.31 Nβ

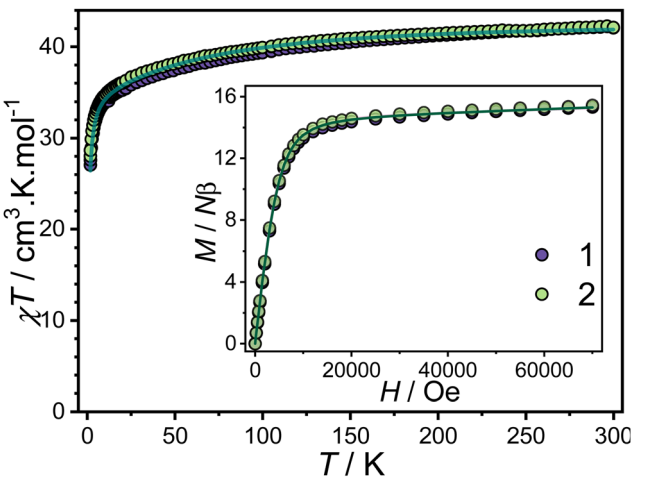

Fig. 2 Temperature dependence of χT under an applied magnetic field of 1000 Oe for **1** and **2**. Inset: Field dependence of the magnetization at 1.8 K. The solid lines represent the fit with POLY_ANISO.

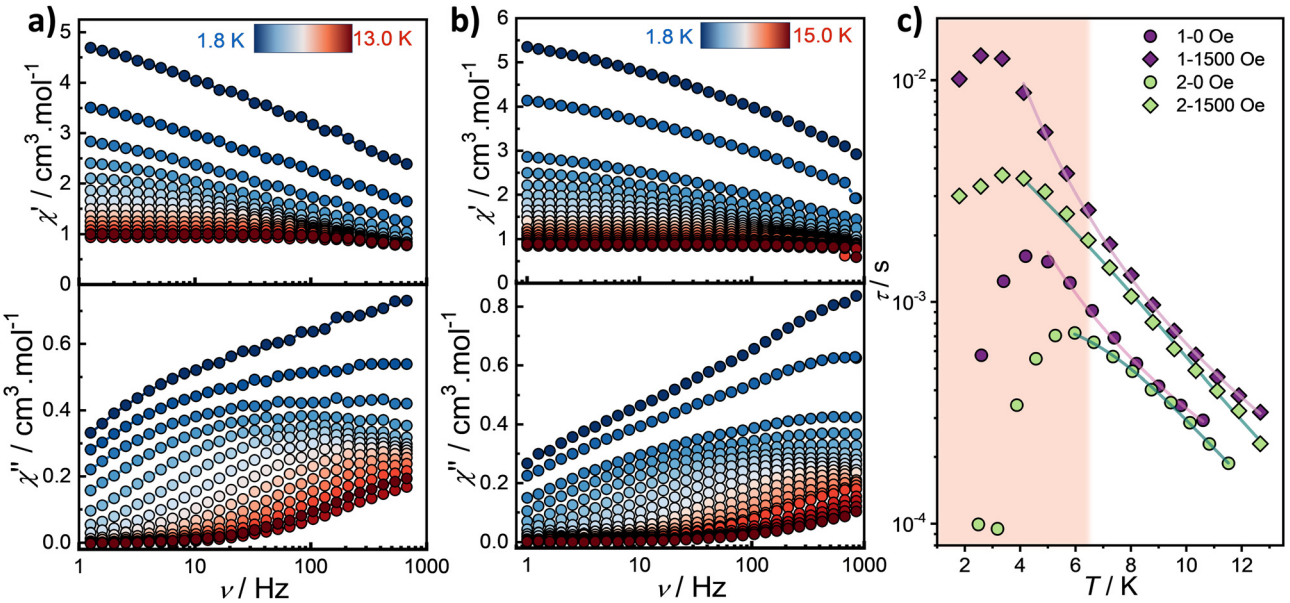

Fig. 3 Frequency dependence of the in-phase (χ') and out-of phase (χ'') susceptibilities for **1** (a) and **2** (b) under a zero dc-field. (c) Temperature dependence of the relaxation time using the ac susceptibility data. The solid line represents the fit. The low temperature regime is highlighted in coral colour.

for **1** and 15.44 Nβ for **2**, consistent with the presence of CF effects.

The magnetic hysteresis loops, measured at 1.8 K, display an opening for both complexes, suggesting the presence of slow relaxation dynamics (Fig. S4, ESI†). Notably, the hysteresis loop for complex **1** is slightly wider compared to that of complex **2**, suggesting distinct relaxation profiles.

The occurrence of slow relaxation of the magnetization was investigated using alternating current (ac) measurements. Under zero dc field, both complexes exhibit a broad out-of-phase (χ'') signal in their ac susceptibility at low temperatures, with no clearly defined maximum (Fig. 3). Upon heating, the signal sharpens, and a single peak gradually emerges up to 13 K.

In the high-temperature regime, the maximum shifts to higher frequencies, as typically expected for systems exhibiting slow relaxation. However, in the low-temperature regime, the opposite behavior is observed, with the maximum shifting to lower frequencies. This unusual trend could arise from the presence of multiple Dy^{3+} crystallographic sites, strong intermolecular interactions or possibly a spin frustrated system which may affect the relaxation dynamics.

While these results are primarily attributed to an intrinsic effect of the molecular triangle, it is important to consider the potential role of intermolecular interactions. However, comparison with our previously reported $[Dy_3(hnc)_3(DMF)_6]$ triangle which shows even larger intermolecular Dy^{3+}–Dy^{3+} separations and lacks solvate molecules,[31] suggests that these are not the dominant factor.

The observed unusual behavior is further confirmed by the Cole–Cole plots, where the data could not be satisfactorily fitted with a generalized Debye model (Fig. S5, ESI†). In the high-temperature regime, the α values remain relatively large until approximately 10 K (about 0.2), indicating a broad distribution of relaxation times (Tables S3 and S4, ESI†). This confirms that the relaxation dynamics are more complex than a simple single relaxation model. The relaxation times, τ, were estimated from the ac data. The temperature dependence of τ clearly confirms the presence of a distinct low-temperature regime, with a decrease of the relaxation time below approximately 6 and 4 K for **1** and **2**, respectively (Fig. 3c). The "high-temperature" thermal dependence of τ can be fitted with a Raman process using

$$\tau^{-1} = CT^n. \quad (1)$$

For complex **2**, a QTM term must be included to obtain a pertinent fit (Fig. 3c). The best fit parameters are provided in Table 2 and highlight also differences in the relaxation dynamics between the two complexes. Note that inclusion a thermally activated behavior leads to unrealistic fitting parameters, suggesting that the dynamics in the high temperature regime is indeed dominated by a Raman relaxation.

As the relaxation dynamics, and in particular the QTM, could be significantly influenced by dc fields, the field dependence of the ac susceptibility was investigated at 2 K (Fig. S6, ESI†).

Table 2 Fit parameters of the temperature dependence of the relaxation time for **1** and **2**

Compound	n	C (s^{-1} K^{-n})	τ_{QTM} (s)	A (s^{-1} K)
1 (0 Oe)	2.34 ± 0.05	14 ± 1	—	—
1 (1500 Oe)	3.06 ± 0.03	1.3 ± 0.1		—
2 (0 Oe)	4.4 ± 0.2	0.09 ± 0.04	(8.6 ± 0.4) × 10^{-4}	—
2 (1500 Oe)	4.6 ± 0.4	0.03 ± 0.02	—	63 ± 12

Both complexes exhibit intricate behavior, with an increase in relaxation time up to approximately 1500–2000 Oe, after which a plateau in χ'' is observed, preventing further analysis of the relaxation time (Fig. S7, ESI†). For direct comparison between the two complexes, a dc field of 1500 Oe was selected to study its effect on the relaxation dynamics. The frequency dependence collected under this dc field reveals a comparable behavior in comparison to the zero-field data but with maximum observed at lower frequency (Fig. S8, ESI†). Subsequent Cole–Cole analysis (Fig. S9 and Tables S5 and S6, ESI†) and extraction of the relaxation time confirm an increase in relaxation time compared to the zero-field data. The temperature dependence of the relaxation time could be modelled in the high temperature regime with a Raman process for complex **1**, while an additional direct process term is needed for complex **2**, using the equation

$$\tau^{-1} = CT^n + AT \quad (2)$$

(Fig. 3c, Table 2). Although the relaxation times for complexes **1** and **2** differ, they exhibit similar temperature-dependent profiles.

The longer relaxation time observed for complex **1** indicates enhanced axiality compared to complex **2**. For a given compound, the relaxation times are comparable under zero-field and dc-field conditions at higher temperatures. At lower temperatures, a clear bifurcation between the zero-field and field-induced relaxation data becomes however apparent.

3.3. Theoretical calculations

To further investigate the relaxation dynamics and explain the observed differences between the complexes, *ab initio* calculations were carried out at the CASSCF level using the ORCA package.[53] For each Dy_3 triangles, two Dy^{3+} ions in the respective crystallographic sites were replaced by diamagnetic Y^{3+} ions, creating Dy_1, Dy_2, and Dy_3 fragments associated with each Dy^{3+} center. The results reveal substantial variations in magnetic anisotropy between the different Dy^{3+} sites, both within individual triangular complexes and across complexes **1** and **2**.

To provide a clearer understanding, we first analyse the electronic structures of the different Dy^{3+} sites in complex **1**, which presents the best magnetic properties. All Dy^{3+} sites exhibit substantial axiality, with g_z values around 19.3 for Dy_1 and Dy_3, and slightly higher for Dy_2 (g_z = 19.57) (Table 3). Wavefunction compositions indicate a dominant contribution (>89%) from the $m_J = |\pm 15/2\rangle$ state for all the sites (Tables S7–S9, ESI†). However, none of the sites could be considered as perfectly axial ($g_z \approx 20$). Furthermore, despite Dy_2's slightly higher axiality, its transverse g_x and g_y components were in the same order of magnitude to those of Dy_1 and Dy_3, as confirmed by the quantitative comparison of QTM rates obtained from SINGLE_ANISO (Fig. 4). The anisotropic axes of the ground KD for the Dy^{3+} sites are nearly perpendicular to the Dy_3 triangular plane (Fig. 5a) but exhibit varying tilt angles (Table S10, ESI†). The angles between the "out-of-plane" phenoxide and "in-plane" phenoxide in association with the Dy-phenoxide bond lengths most likely influence the tilt of the anisotropic axis relative to the Dy_3 triangular plane. The tilting of the anisotropic axes relative to the Dy^{3+}–Dy^{3+} intranuclear vectors varies across the Dy^{3+} sites. Dy_1 shows the most uniform tilting across both Dy_1–Dy_2 and Dy_1–Dy_3 directions, with angles remaining close to perpendicular, while Dy_3 exhibits slightly greater variation. Dy_2, on the other hand, demonstrates the largest angular deviations. These variations in tilt angles emphasize the geometric and electronic diversity among the Dy^{3+} sites, which likely influences the dipolar interactions.

Theoretical calculations also reveal differences in the CF splitting across the different centers. Specifically, the first

Table 3 Energy of the lowest Kramers doublets (KD) and their associated g tensors on the individual Dy fragments for **1**

KD	Energy (cm^{-1}) Dy_1	g tensor Dy_1	Energy (cm^{-1}) Dy_2	g tensor Dy_2	Energy (cm^{-1}) Dy_3	g tensor Dy_3
1	0	g_x = 0.0117	0	g_x = 0.0083	0	g_x = 0.0084
		g_y = 0.0023		g_y = 0.0134		g_y = 0.0170
		g_z = 19.3067		g_z = 19.5708		g_z = 19.3313
2	155	g_x = 0.3623	179	g_x = 0.0083	140	g_x = 0.3296
		g_y = 0.6687		g_y = 0.3186		g_y = 0.6580
		g_z = 15.8018		g_z = 15.8432		g_z = 15.3503
3	247	g_x = 1.5716	253	g_x = 0.7154	204	g_x = 0.7776
		g_y = 2.5509		g_y = 1.6082		g_y = 1.9322
		g_z = 14.5608		g_z = 14.3943		g_z = 14.5719
4	333	g_x = 7.9748	343	g_x = 3.6996	299	g_x = 5.063
		g_y =6.8501		g_y = 5.2254		g_y = 6.1174
		g_z = 4.4915		g_z = 9.9122		g_z = 9.1874
5	412	g_x = 0.3304	418	g_x = 1.4635	377	g_x = 0.0843
		g_y = 3.2666		g_y = 5.4189		g_y = 4.1231
		g_z = 11.3609		g_z = 10.8270		g_z = 11.1017
6	497	g_x = 0.0722	486	g_x = 0.7708	461	g_x = 1.4451
		g_y = 2.3338		g_y = 3.3058		g_y = 3.8186
		g_z = 13.3185		g_z = 14.8958		g_z = 10.9838
7	544	g_x =1.0455	528	g_x = 0.5906	502	g_x = 2.0211
		g_y =1.5273		g_y = 1.2066		g_y = 3.7924
		g_z = 16.1839		g_z = 17.6440		g_z = 13.5665
8	589	g_x = 0.1750	606	g_x = 0.0717	562	g_x = 0.3038
		g_y = 0.3598		g_y = 1.2066		g_y = 0.4998
		g_z = 19.1759		g_z = 18.5462		g_z = 19.0740

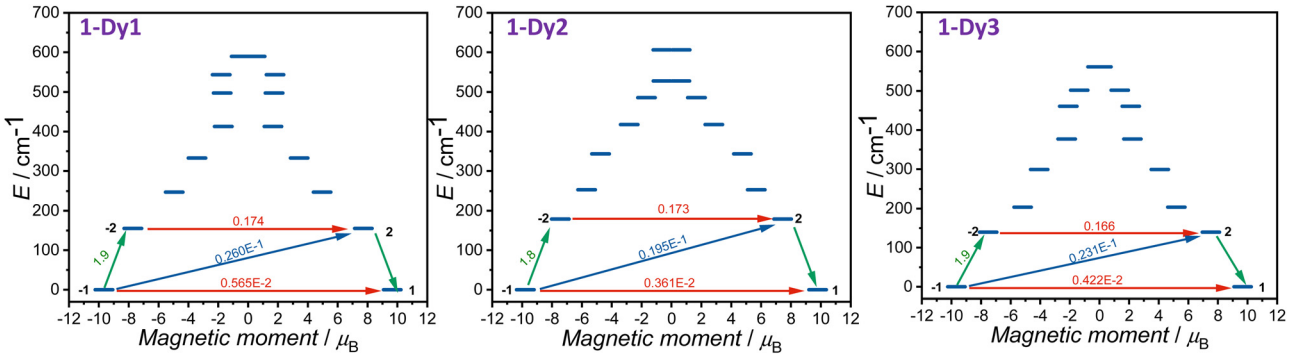

Fig. 4 Energy diagram for low-lying KDs and transition magnetic moment matrix elements[59] (in μB) for the connected states (only for the KD1 and KD2) for fragments **1**. For each KD (*n*), the corresponding states (−*n*, *n*) are placed according to their magnetic moments. The horizontal arrows show the QTM transitions within each doublet, whereas the non-horizontal arrows are spin-phonon transition paths. Only the first KDs are shown here.

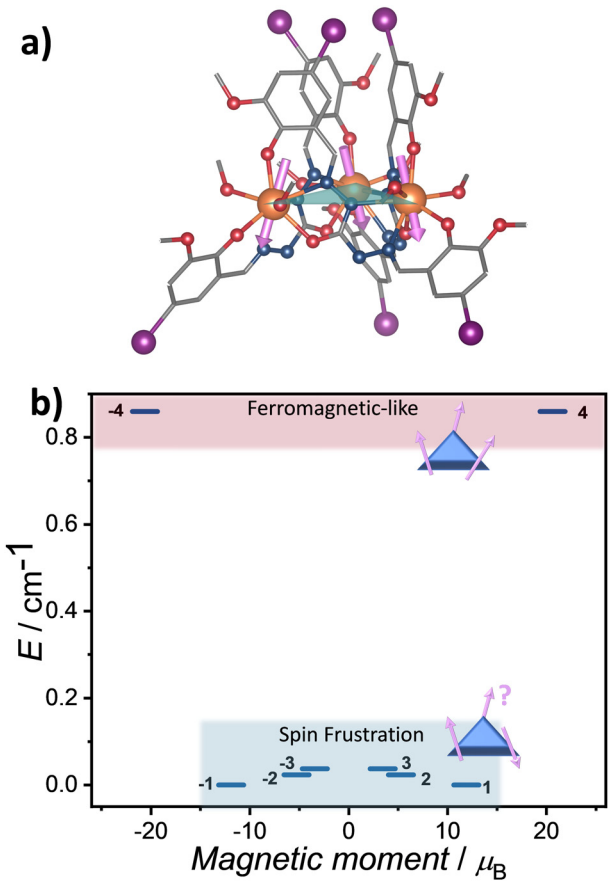

Fig. 5 (a) Orientation of the anisotropic axis (pink) corresponding to the ground KD in **1**. (b) Energy diagram of the coupled states resulting from the dipolar interactions in **1**.

excited KD level ranges from 140 cm^{-1} (Dy_3) to 179 cm^{-1} (Dy_2) (Fig. 4 and Table 3). Despite these significant splitting values, a Raman-mediated relaxation is observed, likely due to the limited axiality of both the ground and 1st excited KD for all the Dy^{3+} sites.

Although this analysis points out substantial differences between the Dy^{3+} sites, the effect of magnetic interaction was also investigated. Since the local magnetic anisotropy is stronger than the magnetic interactions and nearly perpendicular to the Dy_3 plane, this system corresponds to a case of Ising spin frustration, characterized by a six-fold degenerate ground state composed of two aligned spins and one inverted spin. To validate this, POLY_ANISO was employed to obtain details about the magnetic interactions between the Dy^{3+} sites. Given the large Dy^{3+}–Dy^{3+} intramolecular distances (>5.7 Å) and the substantial number of bridging atoms, exchange interactions were neglected, and only dipolar interactions were considered.[34] This allows to nicely reproduce the χT *vs.* *T* and *M* *vs.* *H* curves (Fig. 3 and Fig. S10, ESI†). The calculated dipolar interaction matrix (Table S10, ESI†) for **1** suggests a frustrated system. The six-fold degenerate ground state, characterized by two aligned spins and one inverted spin, splits into three closely spaced doublets, located at 0, 0.023, and 0.037 cm^{-1}, whereas the excited ferromagnetic state is predicted at 0.859 cm^{-1} (Fig. 5b and Table S12, ESI†). Such small energy differences between the three ground doublets are typically regarded as a hallmark of frustration in triangular systems.[38–40,60]

The computed energy spectrum and corresponding g_z values provide critical insights into the nature of the coupled states within the Dy_3 triangle (Fig. 5b). The three low-lying doublets exhibit close g_z values ranging between 21.52 to 24.45 (Table S12, ESI†). However, their corresponding magnetic moments differ, suggesting varying degrees of spin canting in each state (Fig. 5b). In the ground state, the spins exhibit a moderate degree of canting, resulting in an intermediate magnetic moment of approximately 11.9 μB.

The second and third doublets also correspond to frustrated configurations, where the canting becomes more pronounced, leading to further reductions in the magnetic moments (5.3 μB and 3.4 μB, respectively). Lastly, the fourth state represents a ferromagnetic-like configuration, yet the spins remain canted rather than perfectly aligned, yielding a reduced magnetic moment of 20.6 μB instead of the expected ∼30 μB for three Ising-like Dy^{3+} ions with ferromagnetic coupling in the absence of canting.

In comparison to **1**, the electronic structures of the Dy^{3+} centers in **2** exhibit notable disparities (Tables S13–S16, ESI†).

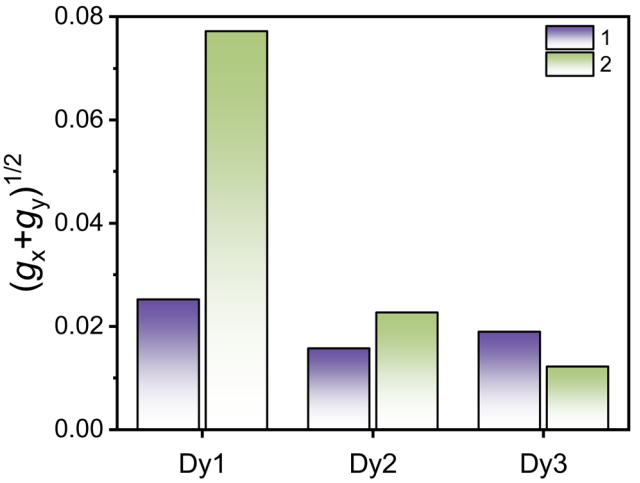

Fig. 6 Bar plot showing the transversal magnetic anisotropy determined by the computed $\sqrt{g_x^2+g_y^2}$ for the different Dy^{3+} sites in **1** and **2**.

In particular, Dy_1 exhibits the lowest axiality with a g_z value of 19.05 whereas Dy_3 shows the greatest axiality (g_z = 19.62). This trend is also reflected in the ground-state wavefunction composition where Dy_1 shows only 84% of $m_J = |\pm 15/2\rangle$ state, in contrast to Dy_2 and Dy_3 which exhibit 92.6% and 94.4%, respectively (Tables S13–S16, ESI†). Hence, the degree of axiality progressively increases from Dy_1 to Dy_3, as also mirrored by energies of the first KD found at 111, 159 and 177 cm^{-1} for Dy_1, Dy_2 and Dy_3, respectively. The orientation of the anisotropic axes (Fig. S11, ESI†) and their tilting relative to the Dy_3 plane are comparable to those observed in **1** (Table S10, ESI†).

However, Dy_1 exhibits notably higher computed QTM rates (Fig. S12, ESI†), further corroborated by the transverse components of the *g*-tensor for the ground doublet. The transverse *g*-tensor component, proportional to $\sqrt{g_x^2+g_y^2}$,[61] highlights the larger transverse anisotropy of Dy_1 compared to Dy_2 and Dy_3, as well as to the Dy^{3+} sites present in complex **1** (Fig. 6).

It turns out that with the exception of the Dy_3 site, the transverse components are consistently greater in **2**, especially for Dy_1. The enhanced transverse components in **2** likely contribute to its reduced SMM performance compared to **1**.

The site-dependent influence of the halogen substituent on the Dy^{3+} electronic structure complicates the identification of a clear trend across the series, highlighting the subtle interplay of electronic and steric effects. Future studies focusing on systems with a single Dy^{3+} site could help isolate the direct impact of the halogen and potentially reveal more general trends. Additionally, investigating unsubstituted or differently substituted analogues would further elucidate these effects. On the other hand, analysis using POLY_ANISO reveals a comparable exchange spectrum between **1** and **2**, with the presence of spin frustration (Fig. S13 and Table S12, ESI†).

All these findings suggest that the relaxation dynamics is predominantly of single-ion origin. Indeed, the weak degeneracy breaking of the spin-frustrated states should enable the thermal population of these states, even at low temperatures. Additionally, the conversion between the frustrated states could occur through a single spin flip on one Dy^{3+} center.[39] Therefore, the relaxation dynamics shall be most likely predominantly governed by single-ion effects. Furthermore, the fact that none of the Dy^{3+} sites are highly axial is also consistent with the observed Raman relaxation processes at high temperatures and further supports the single-ion origin of the magnetic dynamics in these triangular Dy_3 complexes.

Nevertheless and to our knowledge, previous examples of frustrated Dy-based Ising triangles do not show the low temperature regime in the ac relaxation profile as observed in **1** and **2**. While it is tempting to attribute this behavior to distinct relaxation pathways arising from the different Dy^{3+} crystallographic sites or possible intermolecular interactions, the comparison with our previously reported Dy_3 triangle $[Dy_3(hnc)_3(DMF)_6]$ (H_3-hnc: 1,5-bis(2-hydroxy-3-methoxy-5 nitrobenzylidene) carbonohydrazide) suggests a more complex picture. Unlike **1** and **2**, this compound features a unique crystallographic Dy^{3+} site related by a C_3 axis, and also exhibits a drop in relaxation time at low temperatures (Fig. S14, ESI†). To gain further insights, we performed CASSCF calculations to elucidate the electronic structure of $[Dy_3(hnc)_3(DMF)_6]$. Despite differences in substituents and coordinated solvents (MeOH *vs.* DMF), the CF splitting appears comparable to that in **1** and **2**, with a first excited KD located at 117 cm^{-1}, while the KD ground-state shows g_z = 19.51 (Table S17 and Fig. S15, ESI†). In $[Dy_3(hnc)_3(DMF)_6]$, the alignment of the anisotropic axes is influenced by the unique crystallographic Dy^{3+} site, leading to a less pronounced tilt between the relative axes compared to **1** and **2** (Fig. S16, ESI†). When considering only dipolar interactions, the calculated energy spectrum is closely resembling those of **1** and **2**, displaying three degenerated doublets and a ferromagnetic excited state around 0.86 cm^{-1}. Furthermore, the significantly large intermolecular Dy^{3+}–Dy^{3+} distances in $[Dy_3(hnc)_3(DMF)_6]$ (exceeding 15 Å) suggest that intermolecular interactions are unlikely to drive the low-temperature behavior observed across the Dy_3 triangles.

To summarize, our findings suggest that single-ion anisotropy likely governs the relaxation behavior in our systems. The moderate magnetic axiality of the Dy^{3+} centers is consistent with the observed Raman relaxation processes in the high-temperature range; however, distinct behaviors are observed across the series, including the previously reported compound. This underscores the influence of the substituent and symmetry on the relaxation dynamics. While our analysis using POLY_ANISO indicates the presence of spin frustration driven by dipolar interactions, as evidenced by the closely spaced ground doublets in the energy spectrum, the direct attribution of the unusual relaxation behavior observed at low temperatures to this phenomenon warrants further investigation, as distinct relaxation pathways arising from the different Dy^{3+} sites and/or subtle lattice effects might also contribute to this low-temperature regime. These findings emphasize the need for future research to better capture the underlying dynamics and explore potential avenues for enhancing the magnetic axiality to improve the SMM performance of such frustrated triangular Dy_3 complexes.

4. Conclusions

In this study, we have investigated a series of triangular Dy_3 tripod-like complexes that represent rare examples of Ising spin frustration in a Dy_3 triangle. The unique topology, combined with the nearly perpendicular orientation of the principal magnetic axes to the triangle's plane, leads to a frustrated ground state driven by dipolar interactions, with minimal influence from exchange interactions. This work highlights the critical importance of precise geometric and anisotropic control in achieving such frustration, providing a valuable model for understanding magnetic phenomena in triangular systems.

Remarkably, we observe a distinctive slow relaxation regime at low temperatures in both complexes. While spin frustration is present, its influence on the relaxation dynamics should be limited, with the single-ion effects dominating the high-temperature behavior, highlighting the delicate balance between these two mechanisms. However, comparison with a similar Dy_3 triangle featuring a unique Dy^{3+} ion, suggests a more intricate relaxation mechanism at low temperature. Additionally, we demonstrate that halogen substitution at the *para* position of the ligands influences the relaxation dynamics. The halogen substituents modulate the local crystal field, thereby affecting the magnetic anisotropy of the Dy^{3+} centers. However, this modulation exhibits site-specific variations within the Dy_3 triangle, reflecting the complex interplay of steric and electronic factors in the ligand environment.

The presence of spin frustration opens promising avenues for future exploration, particularly in fine-tuning the magnetic properties of triangular SMMs through strategic modifications of the ligand framework (including substituents) and by employing techniques such as solvent exchange or other post-synthetic modifications.

Data availability

Crystallographic data for **1** and **2** has been deposited at the Cambridge Crystallographic Data Centre as Supplementary Publication No 2412859 and 2412858.†

Conflicts of interest

There are no conflict of interest to declare.

Acknowledgements

The authors thank the University of Montpellier, CNRS. J. Long also acknowledges the support from the Institut Universitaire de France. We also gratefully acknowledge the financial support from National Chung Hsing University and the National Science and Technology Council, Taiwan 113-2113-M-005-006 to P.-H. Lin.

Notes and references

1 J. Luzon and R. Sessoli, *Dalton Trans.*, 2012, **41**, 13556–13567.
2 D. N. Woodruff, R. E. P. Winpenny and R. A. Layfield, *Chem. Rev.*, 2013, **113**, 5110–5148.
3 F. Troiani and M. Affronte, *Chem. Soc. Rev.*, 2011, **40**, 3119–3129.
4 L. Bogani, A. Vindigni, R. Sessoli and D. Gatteschi, *J. Mater. Chem.*, 2008, **18**, 4750–4758.
5 R. A. Layfield and M. Murugesu, *Lanthanides and Actinides in Molecular Magnetism*, Wiley, 2015.
6 J.-L. Liu, Y.-C. Chen and M.-L. Tong, *Chem. Soc. Rev.*, 2018, **47**, 2431–2453.
7 R. A. Layfield, *Organometallics*, 2014, **33**, 1084–1099.
8 C. A. P. Goodwin, F. Ortu, D. Reta, N. F. Chilton and D. P. Mills, *Nature*, 2017, **548**, 439–442.
9 F.-S. Guo, B. M. Day, Y.-C. Chen, M.-L. Tong, A. Mansikkamäki and R. A. Layfield, *Science*, 2018, **362**, 1400–1403.
10 K. Randall McClain, C. A. Gould, K. Chakarawet, S. J. Teat, T. J. Groshens, J. R. Long and B. G. Harvey, *Chem. Sci.*, 2018, **9**, 8492–8503.
11 J. Liu, Y.-C. Chen, J.-L. Liu, V. Vieru, L. Ungur, J.-H. Jia, L. F. Chibotaru, Y. Lan, W. Wernsdorfer, S. Gao, X.-M. Chen and M.-L. Tong, *J. Am. Chem. Soc.*, 2016, **138**, 5441–5450.
12 Y.-S. Ding, N. F. Chilton, R. E. P. Winpenny and Y.-Z. Zheng, *Angew. Chem., Int. Ed.*, 2016, **55**, 16071–16074.
13 Y.-S. Ding, K.-X. Yu, D. Reta, F. Ortu, R. E. P. Winpenny, Y.-Z. Zheng and N. F. Chilton, *Nat. Commun.*, 2018, **9**, 3134.
14 Y. S. Ding, T. Han, Y. Q. Zhai, D. Reta, N. F. Chilton, R. E. P. Winpenny and Y. Z. Zheng, *Chem. – Eur. J.*, 2020, **26**, 5893–5902.
15 K.-X. Yu, J. G. Kragskow, Y.-S. Ding, Y.-Q. Zhai, D. Reta, N. F. Chilton and Y.-Z. Zheng, *Chem*, 2020, **6**, 1777–1793.
16 V. Parmar, D. P. Mills and R. Winpenny, *Chem. – Eur. J.*, 2021, **27**, 7625–7645.
17 J. Long, A. O. Tolpygin, E. Mamontova, K. A. Lyssenko, D. Liu, M. D. Albaqami, L. F. Chibotaru, Y. Guari, J. Larionova and A. A. Trifonov, *Inorg. Chem. Front.*, 2021, **8**, 1166–1174.
18 X.-L. Ding, Y.-Q. Zhai, T. Han, W.-P. Chen, Y.-S. Ding and Y.-Z. Zheng, *Chem. – Eur. J.*, 2021, **27**, 2623–2627.
19 W. J. Xu, Q. C. Luo, Z. H. Li, Y. Q. Zhai and Y. Z. Zheng, *Adv. Sci.*, 2024, **11**, e2308548.
20 A. Lunghi, F. Totti, R. Sessoli and S. Sanvito, *Nat. Commun.*, 2017, **8**, 14620.
21 L. Escalera-Moreno, J. J. Baldoví, A. Gaita-Ariño and E. Coronado, *Chem. Sci.*, 2018, **9**, 3265–3275.
22 D. Reta, J. G. C. Kragskow and N. F. Chilton, *J. Am. Chem. Soc.*, 2021, **143**, 5943–5950.
23 Y.-C. Chen and M.-L. Tong, *Chem. Sci.*, 2022, **13**, 8716–8726.
24 M. J. Giansiracusa, E. Moreno-Pineda, R. Hussain, R. Marx, M. Martínez Prada, P. Neugebauer, S. Al-Badran, D. Collison, F. Tuna, J. van Slageren, S. Carretta, T. Guidi, E. J. L. McInnes, R. E. P. Winpenny and N. F. Chilton, *J. Am. Chem. Soc.*, 2018, **140**, 2504–2513.
25 R. J. Blagg, L. Ungur, F. Tuna, J. Speak, P. Comar, D. Collison, W. Wernsdorfer, E. J. L. McInnes, L. F. Chibotaru and R. E. P. Winpenny, *Nat. Chem.*, 2013, **5**, 673–678.
26 J. Long, F. Habib, P.-H. Lin, I. Korobkov, G. Enright, L. Ungur, W. Wernsdorfer, L. F. Chibotaru and M. Murugesu, *J. Am. Chem. Soc.*, 2011, **133**, 5319–5328.

27 K. Katoh, R. Asano, A. Miura, Y. Horii, T. Morita, B. K. Breedlove and M. Yamashita, *Dalton Trans.*, 2014, **43**, 7716–7725.
28 E. M. Pineda, Y. Lan, O. Fuhr, W. Wernsdorfer and M. Ruben, *Chem. Sci.*, 2017, **8**, 1178–1185.
29 J. Xiong, H.-Y. Ding, Y.-S. Meng, C. Gao, X.-J. Zhang, Z.-S. Meng, Y.-Q. Zhang, W. Shi, B.-W. Wang and S. Gao, *Chem. Sci.*, 2017, **8**, 1288–1294.
30 J. D. Rinehart, M. Fang, W. J. Evans and J. R. Long, *Nat. Chem.*, 2011, **3**, 538–542.
31 L.-W. Cheng, C.-L. Zhang, J.-Y. Wei and P.-H. Lin, *Dalton Trans.*, 2019, **48**, 17331–17339.
32 Y.-S. Meng, Y.-S. Qiao, M.-W. Yang, J. Xiong, T. Liu, Y.-Q. Zhang, S.-D. Jiang, B.-W. Wang and S. Gao, *Inorg. Chem. Front.*, 2020, **7**, 447–454.
33 L. Ungur, S.-Y. Lin, J. Tang and L. F. Chibotaru, *Chem. Soc. Rev.*, 2014, **43**, 6894–6905.
34 L. F. Chibotaru, L. Ungur and A. Soncini, *Angew. Chem., Int. Ed.*, 2008, **47**, 4126–4129.
35 J. Tang, I. Hewitt, N. T. Madhu, G. Chastanet, W. Wernsdorfer, C. E. Anson, C. Benelli, R. Sessoli and A. K. Powell, *Angew. Chem., Int. Ed.*, 2006, **45**, 1729–1733.
36 J. Luzon, K. Bernot, I. J. Hewitt, C. E. Anson, A. K. Powell and R. Sessoli, *Phys. Rev. Lett.*, 2008, **100**, 247205.
37 Y.-X. Wang, Y. Zhou, Y. Ma, P. Lu, Y.-Q. Zhang, Y. Sun and P. Cheng, *Adv. Sci.*, 2024, **11**, 2308220.
38 V. Vieru, L. Ungur and L. F. Chibotaru, *J. Phys. Chem. Lett.*, 2013, **4**, 3565–3569.
39 T. Pugh, F. Tuna, L. Ungur, D. Collison, E. J. L. McInnes, L. F. Chibotaru and R. A. Layfield, *Nat. Commun.*, 2015, **6**, 7492.
40 G. Lu, Y. Liu, W. Deng, G.-Z. Huang, Y.-C. Chen, J.-L. Liu, Z.-P. Ni, M. Giansiracusa, N. F. Chilton and M.-L. Tong, *Inorg. Chem. Front.*, 2020, **7**, 2941–2948.
41 A. P. Orlova, J. D. Hilgar, M. G. Bernbeck, M. Gembicky and J. D. Rinehart, *J. Am. Chem. Soc.*, 2022, **144**, 11316–11325.
42 M. G. Bernbeck, A. P. Orlova, J. D. Hilgar, M. Gembicky, M. Ozerov and J. D. Rinehart, *J. Am. Chem. Soc.*, 2024, **146**, 7243–7256.
43 M. Andruh, *Dalton Trans.*, 2015, **44**, 16633–16653.
44 J. Long, Y. Guari, R. A. S. Ferreira, L. D. Carlos and J. Larionova, *Coord. Chem. Rev.*, 2018, **363**, 57–70.
45 J. Long, *Front. Chem.*, 2019, **7**, 63.
46 J.-H. Jia, Q.-W. Li, Y.-C. Chen, J.-L. Liu and M.-L. Tong, *Coord. Chem. Rev.*, 2019, **378**, 365–381.
47 J. Tang and P. Zhang, *Lanthanide Single Molecule Magnets*, Springer Berlin Heidelberg, Berlin, Heidelberg, 2015, pp. 41–90, DOI: 10.1007/978-3-662-46999-6_2.
48 S. T. Liddle and J. van Slageren, *Chem. Soc. Rev.*, 2015, **44**, 6655–6669.
49 Z. Zhu, M. Guo, X.-L. Li and J. Tang, *Coord. Chem. Rev.*, 2019, **378**, 350–364.
50 J. Long, M. S. Ivanov, V. A. Khomchenko, E. Mamontova, J.-M. Thibaud, J. Rouquette, M. Beaudhuin, D. Granier, R. A. S. Ferreira, L. D. Carlos, B. Donnadieu, M. S. C. Henriques, J. A. Paixão, Y. Guari and J. Larionova, *Science*, 2020, **367**, 671.
51 D. Y. Kim and H. J. Kim, *Org. Lett.*, 2021, **23**, 5256–5260.
52 K. R. More and R. S. Mali, *Tetrahedron*, 2016, **72**, 7496–7504.
53 F. Neese, *Wiley Interdiscip. Rev.:Comput. Mol. Sci.*, 2012, **2**, 73–78.
54 F. Neese, *Wiley Interdiscip. Rev.: Comput. Mol. Sci.*, 2022, **12**, e1606.
55 M. I. Aroyo, J. M. Perez-Mato, C. Capillas, E. Kroumova, S. Ivantchev, G. Madariaga, A. Kirov and H. Wondratschek, *Z. Kristallogr.*, 2006, **221**, 15–27.
56 M. I. Aroyo, A. Kirov, C. Capillas, J. M. Perez-Mato and H. Wondratschek, *Acta Crystallogr., Sect. A: Found. Crystallogr.*, 2006, **62**, 115–128.
57 L. F. Chibotaru and L. Ungur, *The computer programs SINGLE_ANISO and POLY_ANISO*, University of Leuven, **2**, 2006.
58 D. Casanova, M. Llunell, P. Alemany and S. Alvarez, *Chem. – Eur. J.*, 2005, **11**, 1479–1494.
59 L. Ungur and L. F. Chibotaru, *Inorg. Chem.*, 2016, **55**, 10043–10056.
60 R. Grindell, V. Vieru, T. Pugh, L. F. Chibotaru and R. A. Layfield, *Dalton Trans.*, 2016, **45**, 16556–16560.
61 Y. Gil, A. Castro-Alvarez, P. Fuentealba, E. Spodine and D. Aravena, *Chem. – Eur. J.*, 2022, **28**, e202200336.